Cell-specific *Dyt1* ΔGAG knock-in to basal ganglia and cerebellum reveal differential effects on motor behavior and sensorimotor network function

B.J. Wilkes[a], **R.Z. Adury**[a], **D. Berryman**[b], **L.R. Concepcion**[a], **Y. Liu**[b], **F. Yokoi**[b], **C. Maugee**[b], **Y. Li**[b], **D.E. Vaillancourt**[a,b,c]

[a.]Department of Applied Physiology and Kinesiology, University of Florida, Gainesville, FL, USA

[b.]Norman Fixel Institute for Neurological Diseases, Department of Neurology, University of Florida, Gainesville, FL, USA

[c.]Department of Biomedical Engineering, University of Florida, Gainesville, FL, USA

Abstract

Dystonia is a neurological movement disorder characterized by repetitive, unintentional movements and disabling postures that result from sustained or intermittent muscle contractions. The basal ganglia and cerebellum have received substantial focus in studying DYT1 dystonia. It remains unclear how cell-specific ΔGAG mutation of torsinA within specific cells of the basal ganglia or cerebellum affects motor performance, somatosensory network connectivity, and microstructure. In order to achieve this goal, we generated two genetically modified mouse models: in model 1 we performed *Dyt1* ΔGAG conditional knock-in (KI) in neurons that express dopamine-2 receptors (D2-KI), and in model 2 we performed *Dyt1* ΔGAG conditional KI in Purkinje cells of the cerebellum (Pcp2-KI). In both of these models, we used functional magnetic resonance imaging (fMRI) to assess sensory-evoked brain activation and resting-state functional connectivity, and diffusion MRI to assess brain microstructure. We found that D2-KI mutant mice had motor deficits, abnormal sensory-evoked brain activation in the somatosensory cortex, as well as increased functional connectivity of the anterior medulla with cortex. In contrast, we found that Pcp2-KI mice had improved motor performance, reduced sensory-evoked brain activation in the striatum and midbrain, as well as reduced functional connectivity of the striatum with the anterior medulla. These findings suggest that (1) D2 cell-specific *Dyt1* ΔGAG mediated torsinA dysfunction in the basal ganglia results in detrimental effects on the sensorimotor network and motor output, and (2) Purkinje cell-specific *Dyt1* ΔGAG mediated torsinA dysfunction in the cerebellum results in compensatory changes in the sensorimotor network that protect against dystonia-like motor deficits.

Corresponding Author: Bradley J. Wilkes, Ph.D., Department of Applied Physiology and Kinesiology, University of Florida, P.O. Box 118205, Gainesville, FL, 32611, Phone: (352) 294-1767, bwilkes@ufl.edu.

1. Introduction

Dystonia is a neurological movement disorder characterized by repetitive, unintentional movements and disabling postures stemming from sustained or intermittent muscle contractions (Albanese et al., 2013). Dystonia embodies a number of clinical syndromes, including focal dystonia to specific body parts, or generalized dystonia affecting a majority of the body which together represent. Collectively, dystonia represents the third most common movement disorder. The etiology of dystonia can be idiopathic or inherited through known genetic factors. Early-onset generalized DYT1 dystonia is a heterozygous autosomal dominant condition linked to an in-frame GAG mutation of the *TOR1A/DYT1* gene, which causes misfolding of the TorsinA protein, and is the most common genetic type of dystonia (Ozelius et al., 1997).

The basal ganglia and cerebellum have received substantial focus in the study of DYT1 dystonia. A commonly used medication used in people with DYT1 dystonia is trihexyphenidyl, a cholinergic antagonist. Studies have shown that only 60–70% of patients show significant treatment effects from trihexyphenidyl and there can be difficult side-effects for patients when on the medication (Burke et al., 1986; Fahn, 1983). Although abnormal cholinergic dynamics are observed in the basal ganglia and cerebellum in association with DYT1 dystonia (Mazere et al., 2021; Xing et al., 2022), a number of studies suggest that non-cholinergic cell types may also play an important role in the pathophysiology of dystonia (Hayashi et al., 2008; Lee et al., 2014; Liu et al., 2020; Maltese et al., 2014; Miyazaki, 2012).

The most consistent structural alterations found in human neuroimaging studies of dystonia similarly implicate the basal ganglia and cerebellum (for a review, see MacIver et al., 2022). Regional brain volume differences in dystonia have primarily been identified in the basal ganglia, whereas studies of white matter with diffusion tensor imaging (DTI) have revealed reduced integrity in the cerebellothalamocortical tract that correlated with motor network activity (Miklos Argyelan et al., 2009; Carbon et al., 2008). Although both nonmanifesting and clinically manifesting DYT1 mutation carriers show these white matter abnormalities proximal to the cerebellum, nonmanifesting mutation carriers have an additional region of white matter tract changes in distal portions of this tract near the thalamus, possibly representing a secondary compensatory change in those without clinically manifesting dystonia (Miklos Argyelan et al., 2009).

Research in transgenic animal models has also greatly increased our understanding of torsinA dysfunction. Broadly speaking, *Dyt1* knock-out (KO) models provide insights about reduced levels of endogenous torsinA, whereas *Dyt1* GAG knock-in (KI) models help to understand the effects of mutant torsinA analogous to the protein mutation observed in people with early-onset DYT1 dystonia (Dang et al., 2005; Sharma et al., 2005;

Shashidharan et al., 2005). Homozygous models of torsinA dysfunction are nonviable or show neonatal lethality, but heterozygous *Dyt1* KO and KI models may display dystonic postures or subtle motor deficits, paired with other pathophysiological features of dystonia. The *Dyt1* ΔGAG KI mouse model is one of the most widely studied genetic models of dystonia and recapitulates many features of DYT1 dystonia, including motor behavior deficits and abnormal muscle contractions observed with electromyography, and altered brain microstructure (Dang et al., 2005; DeAndrade et al., 2016). Similar to humans with DYT1 dystonia, *Dyt1* ΔGAG KI mice also exhibit microstructural alterations in both basal ganglia and cerebellar circuitry (Song et al., 2014, 2013; Uluǧ et al., 2011).

Although studying the basal ganglia and cerebellum independently has greatly increased our understanding of mechanisms contributing to the pathophysiology of dystonia, it has been suggested that dystonia may be best viewed as a functional network disorder, where there is disrupted flow and integration of signals across multiple components of the sensorimotor network (Burciu et al., 2017; DeSimone et al., 2017; Simonyan, 2018). Therefore, considering dystonia to be a product of either basal ganglia or cerebellar dysfunction is likely a false conceptual perspective. What is lacking from this perspective is a more comprehensive understanding of how torsinA dysfunction in specific cell types contributes to dystonia-related phenotypes and changes in sensorimotor network pathophysiology and connectivity. Moreover, evaluating the effects of cell-specific torsinA dysfunction *in vivo* enables assessment of network properties not evident when such components are studied separately, and may provide key insights into the clinical and neurophysiological deficits in dystonia (Hallett, 1995; Martella et al., 2014, 2009; Quartarone and Hallett, 2013).

In this study, we sought to identify the impact of torsinA mutation in specific cells in the basal ganglia or cerebellum and their corresponding effects on network-level connectivity and microstructure. To accomplish this goal, we generated two cell-specific *Dyt1* mouse models. In model 1 neurons that express dopamine-2 receptors have *Dyt1* ΔGAG conditional KI (D2-KI), which include medium spiny neurons of the indirect pathway, striatal cholinergic interneurons, and dopaminergic neurons of the basal ganglia. In model 2, neurons that express Purkinje cell protein-2 have *Dyt1* ΔGAG conditional KI (Pcp2-KI), which include Purkinje cells of the cerebellum. In both of these models, we assessed motor behavior and performed *in vivo* neuroimaging at ultra-high field (11.1 T). We used functional magnetic resonance imaging (fMRI) to assess sensory-evoked brain activation and connectivity, along with diffusion tensor imaging (DTI) to assess microstructural changes. The rationale for using *in vivo* sensory-evoked fMRI is that there is prior clinical and neurophysiological evidence demonstrating somatosensory processing deficits in dystonia patients (Hallett, 1995). In particular, there is evidence thermal sensory processing deficits in patients with focal dystonia (Suttrup et al., 2011) and Dyt1 ΔGAG knock-in mice (Scuteri et al., 2021). Our previous work using this methodology has also demonstrated that it is sensitive at detecting subtle deficits in the sensorimotor network (Chu et al., 2020; Wilkes et al., 2021). We evaluated the microstructure of brain regions in the sensorimotor network with DTI because this technique has shown promise in studying neurodegeneration in human conditions and animal models (Burciu et al., 2017; Chu et al., 2020; Colon-Perez et al., 2019; DeSimone et al., 2017). We hypothesized that D2-KI mice would show motor deficits and altered sensorimotor network properties, due to the impact

on torsinA across multiple cell types in the basal ganglia and the critical role those cell types play in the pathophysiology of dystonia. We hypothesized that Pcp2-KI mice would not have motor deficits but would show compensatory brain changes within the sensorimotor network, as informed by our prior work in the Purkinje cell-specific *Dyt1* KO model (Yokoi et al., 2012; Zhang et al., 2011) and imaging findings in the cerebellothalamic tract that distinguish nonmanifesting and clinically manifesting DYT1 mutation carriers (Argyelan et al., 2009).

2.   Materials and methods

2.1   Experimental Design

This study included two dystonia mouse models. In both models, *Dyt1* GAG knock-in was driven by a promoter specific to the cell type that was targeted. In model 1, we targeted neurons of the basal ganglia using the dopamine-2 (*D2*) receptor gene as a promoter (Yokoi et al., 2020) – hereafter referred to as D2-KI. Although D2 receptors exist in other brain regions, in mice the DRD2 BA-Cre mediated recombination is highest in the striatum and low in other brain regions (Gong et al., 2007). In model 2, we targeted cerebellar Purkinje cells using the Purkinje cell protein-2 (*Pcp2*) gene as a promoter (Lyu et al., 2020) – hereafter referred to as Pcp2-KI. Mice from both D2-KI and Pcp2-KI cohorts were generated on the C57BL/6 background strain. We used litter-mate control groups specific to each model to minimize the effects of background strain and cage-to-cage variability on comparisons of mutant versus control animals. The same animals went through each stage of the experiment. First, motor behavior assessments were performed on all animals and included accelerated rotarod and beam-walking tests. Mice were rested for one week in between these behavioral tests and for one week before neuroimaging. Next, four types of MRI scans were acquired for every animal: an anatomical scan, sensory-evoked fMRI, resting-state fMRI, and diffusion MRI. Experimenters performing behavioral testing and MRI acquisition were blind to which animals belonged to the experimental or control groups for each model. After all testing and data pre-processing were complete, genotyping was performed, and experimenters were unblinded to enable group-wise comparisons. Methods for each aspect of this study are described in detail in the following sections.

2.2   Animals

All experiments were performed in accordance with the National Institutes of Health guide for the care and use of Laboratory animals (NIH Publications No. 8023, revised 1978). The D2-KI cohort included 29 (19 male, 10 female) mice with heterozygous *Dyt1* GAG conditional knock-in to neurons expressing the dopamine-2 receptor (D2Cre+/− Swap+/−) with mean age 304 ± 34 days, and 30 (20 male, 10 female) control mice (D2Cre+/−) with mean age 294 ± 36 days. The Pcp2-KI cohort included 37 (20 male, 17 female) mice with heterozygous *Dyt1* GAG conditional knock-in to cerebellar Purkinje cells (Pcp2Cre+/− Swap+/−) with mean age 203 ± 12 d, and 31 (18 male, 13 female) control mice (Pcp2Cre+/−) with mean age 200 ± 11 d. Four Pcp2-KI mutant (Pcp2Cre+/− Swap+/−) male mice were only included in motor behavior analysis: one was due to respiratory failure during neuroimaging, and three were due to data file corruption. All mice were maintained on a 12-hour light/dark cycle with food and water *ad libitum*. All experiments were approved

and monitored by the Institutional Animal Care and Use Committee at the University of Florida and were conducted in ethical compliance with the USPHS Guide for Care and Use of Laboratory Animals.

2.3 Motor Behavior Tests and Analysis

Locomotor function was evaluated for both the D2-KI cohort (n=59, 30 control mice, 29 D2-KI mutant) and the Pcp2-KI cohort (n=68, 31 control mice, 37 Pcp2-KI mutant) using the elevated beam-walking and accelerated rotarod (Ugo Basile) assessments, previously described by in Wilkes et al. (2021) and Yokoi et al. (2020). The beam-walking test assesses the coordination and balance of mice as they traverse beams of decreasing width and differing shapes. Mice were trained to traverse a medium square beam (14 mm width) across 3 trials each day for 2 consecutive days (6 total training trials). On day 3, mice performed one trial traversing a medium square (14 mm width) and one trial traversing a medium round beam (17 mm diameter). Day 4 included one testing trial traversing a small square (7 mm width) and one trial traversing a small round beam (10 mm diameter). All beams were 100 cm in length and total beam slips were recorded for the middle 80 cm section. The number of hind paw slips on each side was counted by investigators blind to the genotypes.

The accelerated rotarod test assesses the ability of mice to maintain balance and coordination on an accelerating rotating rod. The apparatus started at an initial speed of 4 rpm, and then one mouse was put on a slot before the rod speed was gradually accelerated at a rate of 0.2 rpm/s. The latency to fall was measured with a cutoff time of 3 min at a final rate of 40 rpm. Each mouse was placed in the same slot on the apparatus to minimize variation. Mice were tested on 2 days, with 3 trials per day. Between trials on the same day, mice were given a 1-hour rest interval. Rotarod and beam-walking testing occurred within 15–30 days prior to imaging for all animals.

Data were then tested for normality using the SAS 9.4 statistical package. Both beam-walking and rotarod data were not normally distributed, and thus were analyzed using the non-parametric GENMOD procedure in SAS with a negative binomial distribution (Dang et al., 2005; Wilkes et al., 2021). Two-way interactions between genotype and age, weight, beam, side, trial, and sex were explored first, and if found to be significant, included in the final "reduced" model. Although clinically DYT1 dystonia has no sex predominance (Meoni et al., 2020), the basal ganglia and cerebellum have sexual dimorphism (Raz et al., 2001; Rijpkema et al., 2012). Because our models targeted these brain regions, we checked for any existing sex predominance by performing additional behavioral analysis separately for each sex in beam-walking and rotarod tasks. For beam-walking, our analysis only focused on aggregate performance on the small and medium beams on days 3 and 4 of testing, in order to account for learning effects that may have occurred during training on days 1 and 2. For rotarod analysis, mice remaining on the beam at 180 seconds were censored for survival analysis to determine a marginal hazard ratio. Effects were considered significant at $p <$ 0.05.

2.4 MRI Preparation and Scan Parameters

Animal preparation for MRI was performed as previously described in (Wilkes et al., 2021). Briefly, before scanning mice were induced under general anesthesia via isoflurane delivered through a Surgivet vaporizer (Dublin, OH) and then maintained at 1–1.5% isoflurane for the duration of imaging. Research suggests that sensory neurons in the dorsal horn of the spinal cord that respond to noxious stimuli have relatively spared firing rates under isoflurane anesthesia (Kim et al., 2007). The experimental setup for mouse imaging is depicted in Fig. 1. Respiration was monitored using a respiration pad (SA Instruments, Stony Brook, NY) placed beneath the abdomen. Core body temperature was maintained using an in-house recirculating waterbed heating system and monitored via a thermal rectal probe (SA Instruments, Stony Brook, NY). A 256 mm^2 MR compatible advanced thermal stimulator (ATS) thermode (PATHWAY System, Medoc Advanced Medical Systems, Ramat Yishay, Israel) was affixed to the right plantar hind paw, which delivered heat stimulation during imaging.

MRI data were acquired on an 11.1 Tesla Magnex Scientific 40 cm horizontal magnet (Agilent, Inc. Palo Alto, CA, USA) with RRI BFG-240/120-S6: bore size 120mm, Gmax = 1000 mT/m @325A with 200 μs rise time. B^1 excitation and signal detection were achieved using an in-house 2.5 × 3.5 cm quadrature surface transmit/receive mouse head coil tuned to 470.7 MHz (^{1}H resonance) (AMRIS, University of Florida). Scan sequences were prepared and controlled using ParaVision, Version 6.0.1 (Bruker BioSpin, Billerica, MA). Four types of MRI scans were acquired for every animal: an anatomical scan, sensory-evoked fMRI, resting-state fMRI, and diffusion MRI.

Anatomical T2-weighted images were acquired for spatial normalization using a turbo RARE sequence with the following parameters: TR = 5500 ms; TE = 30 ms; excitation angle = 90°; refocusing angle = 180°; dummy scans = 1; averages = 7; slices = 13; orientation = coronal; thickness = 0.9 mm; gap = 0 mm; FOV = 15 × 15 mm; data matrix = 256 × 256 in-plane.

Sensory-evoked and resting state fMRI scans were acquired using a 2-shot EPI sequence with the following parameters: TR = 2000 ms; TE = 15 ms; repetitions = 360 (sensory-evoked fMRI) or 180 (resting state fMRI); flip angle = 90°; dummy scans = 2; slices = 13; coronal orientation; thickness = 0.9 mm; gap = 0 mm; FOV = 15 × 15 mm; data acquisition matrix = 64 × 64 in-plane.

Diffusion MRI scans were acquired using an EPI sequence with the following parameters: TR = 4000 ms; TE = 19 ms; averages = 4; flip angle = 90°; slices = 17; orientation = coronal; thickness = 0.7 mm; gap = 0 mm; FOV = 15 × 11 mm; data matrix = 128 × 96 in-plane. The following diffusion parameters were used: one non-diffusion weighted b0 images; b-value = 2000 s/mm^2; directions = 46.

2.5 Sensory-evoked fMRI Thermal Stimulation

Acquisition of sensory-evoked fMRI involved heat-induced stimulation of the right plantar hind paw. The PATHWAY System was calibrated such that thermal stimulation was applied in a block paradigm alternating between 60 s at the stimulation temperature (42 °C) and 60

s at the baseline temperature (30 °C), beginning and ending with a 30 s baseline block. The change in temperature between blocks was achieved within 300 ms via a cooling rate of 40 °C/s and a heating rate of 70 °C/s.

2.6 fMRI Preprocessing

Data processing for sensory-evoked and resting-state fMRI scans were performed similar to Chu et al. (2020), using custom-designed UNIX shell scripts with commands from Analysis of Functional NeuroImages (AFNI; Cox, 1996) and Advanced Normalization Tools (ANTs; Avants et al., 2010). The functional MRI processing pipeline was automated and could, therefore, be applied equally and without bias to all scans. We acquired 2 duplicate scans from each type of fMRI paradigm (sensory-evoked and resting state). For sensory-evoked fMRI, the 2 duplicate scans were processed identically and used as a repeated measure within subjects. For resting-state fMRI, we concatenated the data from the 2 duplicate scans, such that resting-state data were analyzed as a single time-series. Data were only excluded from sensory-evoked and resting-state fMRI analysis due to excessive motion that prevented deconvolution of the hemodynamic response function.

The first 5 TRs were removed from each fMRI scan to account for signal equilibration. Outliers within each voxel's time series were identified using 3dToutcount in AFNI, and volumes with more than 5% of the total voxels determined to be outliers were flagged for exclusion during regression. Scan data were then de-spiked, slice-time corrected, corrected for motion and distortion via alignment to the first volume (*3dvolreg,* AFNI), spatially smoothed with a 0.3mm full width half maximum (FWHM) Gaussian kernel, and scaled to have a range of (0,200) and mean of 100. For resting-state fMRI data, we also applied bandpass filtering of the time series between 0.01 to 0.1 Hz. The matrix derived from motion-correction was used to compute a demeaned and derivatives of motion parameters for use as regressors. Volumes in which the Euclidian Norm of the derivative values exceeded 0.5 were flagged for exclusion during regression. Brain masks were created on high-resolution anatomical scans and then registered to the fMRI scan from the same animal in order to remove signal from voxels outside the brain. In order to spatially normalize data, fMRI images from each mouse were registered to the T2-weighted anatomical scan from the same animal, and then to a high-resolution T2-weighted mouse template brain, generated from anatomical scans of 160 mice (Chu et al., 2020). We evaluated 12 regions of interest (ROIs) from key areas of the sensorimotor network, which were selected *a priori* based on their relevance to the pathophysiology of dystonia (DeSimone et al., 2016, 2017; MacIver et al., 2022; Wilkes et al., 2021). Some regions that are pertinent to dystonia were not included for ROI analysis, due to their small size and lack of nearby landmarks for reliable segmentation (*e.g.*, pedunculopontine nucleus). These ROIs are depicted on the mouse anatomical template brain in Fig 2B.

2.7 Sensory-evoked fMRI Analysis

We determined the sensory-evoked hemodynamic response time series using a response function convolved with 20 "tent" or piecewise linear B-spline basis functions which capture the percent signal change for BOLD across time (Saad et al., 2006), spanning 80 s from the onset of each stimulation block. Preprocessed data were regressed to these

simulated tent response functions, with six motion parameters calculated during motion correction also accounted for by including them as regressors of no interest. Volumes flagged with excessive motion by 3dToutcount were censored in this step and excluded from the regression analysis. The β-coefficients of the regressed time series (one for each tent) and the corresponding t-statistics, were the dependent variables at this level of analysis. At this stage of the analysis, 2 control mice from the D2-KI cohort (1 male and 1 female) were excluded due to excessive motion that prevented deconvolution of the hemodynamic response function.

The sensory-evoked fMRI data were then transformed to the mouse T2 template (as described in section 2.6). We extracted values of the 20 β-coefficients representing the hemodynamic response time series from 0–80 seconds after hind paw thermal stimulation, from each of the 12 ROIs. Although hind paw stimulation was performed unilaterally, we evaluated the brain's response to the stimulus bilaterally because unilateral heat stimulation has been shown to result in bilateral blood oxygenation level dependent (BOLD) response in mice (Bosshard et al., 2015; Chu et al., 2020).

For statistical analysis of sensory-evoked fMRI data, we performed repeated measures analysis of covariance for each ROI using SPSS Statistics 27 (IBM; Armonk, New York). Between-subjects factors were genotype and sex, duplicate scans (scan 1 and 2) and the sensory-evoked BOLD time-series were considered as within-subjects factors, and age as a covariate. Our primary interest was the sustained portion of the sensory-evoked signal (20–60s after stimulus onset), and thus the BOLD time-series included for statistical analysis were the corresponding 10 tent functions reflecting the signal change in the time period 20–60s after stimulus onset.

2.8 Resting-state fMRI Analysis

Concatenated and preprocessed resting-state fMRI data were subjected to general linear regression. As with sensory-evoked fMRI scans, volumes flagged with excessive motion by 3dToutcount were censored and excluded from the regression analysis. At this stage of the resting-state fMRI analysis, 1 female control mouse from the D2-KI cohort was excluded due to excessive motion. We then applied additional regressors for the mean signal from cerebrospinal fluid (CSF) and the first-order derivatives of the motion parameters calculated during motion correction as this has been suggested to improve resting-state functional connectivity analysis (Satterthwaite et al., 2013). We then performed seed-to-voxel resting-state functional connectivity analysis. We extracted the mean signal of all voxels within a particular ROI for each time point in the concatenated time-series, which was then correlated with the time-series of each voxel throughout the brain in order to generate a whole brain map of functional connectivity. This was done for each of the 12 ROIs.

For resting-state fMRI data, we analyzed functional connectivity using seed-to-voxel approach. We did not observe significant effects of sex on resting-state functional connectivity and thus applied t-tests at each voxel to identify between-group effects for each cohort. For each of the 12 ROIs, between-group statistics (mutant vs. control) were performed at every voxel in the brain using AFNI. In order to control for false-positives across voxels, a one-sample t-test was performed using AFNI's *Clustsim* bootstrapping

option to advise the cluster-extent threshold. *Clustsim* advises a minimum number of significant (uncorrected) voxels for a cluster to be considered significant while controlling for false-positives at our desired alpha of 0.05 (Cox et al., 2017) and is functionally similar to other approaches for controlling for multiple comparisons. *Clustsim* calculations were performed separately for the D2-KI and Pcp2-KI cohorts using the voxel-level threshold of $p < 0.01$ and nearest neighbor (nn3) clusterization. In accordance with the advised cluster threshold, between-group effects were considered significant ($p_{corrected} < 0.05$) at a minimum cluster size of 12 voxels (0.59 mm^3) for the D2-KI cohort, and also coincidentally a minimum cluster size of 12 voxels (0.59 mm^3) in the Pcp2-KI cohort.

2.9   Diffusion MRI Processing and Analysis

Data processing for diffusion MRI was performed similar to Chu et al. (2020), using custom-designed UNIX shell scripts with commands from AFNI (Cox, 1996), FMRIB Software Library (FSL; Jenkinson et al., 2012) and ANTs (Avants et al., 2010). The diffusion MRI processing pipeline was automated and could, therefore, be applied equally and without bias to all scans. Data were corrected for motion and eddy currents using affine transform with FSL's eddy correct function. Diffusion MRI data for three control mice from the D2-KI cohort and two mutant mice from the Pcp2-KI cohort were discarded due to high motion-related distortions. The resultant transformation matrix was used to rotate diffusion-weighted directions (*i.e.*, b-vectors) accordingly, in order to properly estimate the diffusion tensor and diffusion parameters after eddy correction. Estimation of diffusion parameters was calculated using a two-compartment model to account for partial volume effects of extracellular free-water. We utilized publicly available workflow for single shell free water elimination and estimation of diffusion parameters (https://github.com/sameerd/DiffusionTensorImaging), implemented through MATLAB and the DIPY imaging library in Python 3.6 (Garyfallidis et al., 2014). The resultant maps of free-water (FW) and free-water corrected FA (FA$_T$) were variables of interest for this analysis.

In order to spatially normalize data, FA$_T$ images from each mouse were nonlinearly registered to a FA$_T$ mouse template brain, generated from FA$_T$ maps of 160 mice (Chu et al., 2020). Because diffusion scans had a high in-plane resolution (117 × 115 μm) with a relatively large slice thickness (700 μm), we performed nonlinear registration to the template in a slice-by-slice fashion in order to prevent possible warping between slices. The transformation matrices derived from registration of the FA$_T$ scans to the template were then applied to the FW image from the same animal.

For statistical analysis of diffusion MRI data, we performed multivariate analyses of covariance using SPSS Statistics 27 (IBM; Armonk, New York). Between-subjects factors were genotype and sex, with age as a covariate. We analyzed between group differences in FW and FA$_T$ for the same 12 ROIs that were utilized in fMRI analyses, transformed into diffusion MRI space (Fig 2A). Group effects were considered significant at $p < 0.05$.

3. Results

3.1 D2-KI motor deficits and Pcp2-KI motor improvements

For the D2-KI cohort there was a significant genotype effect, such that mutant mice had increased in average beam-walking slips ($p = 0.039$) compared to controls (Fig. 3A; Table 1). There were no significant interactions of genotype with age, weight, beam type, side, trial, batch, or sex (Supplementary Table 1A), and as such these factors were not included in the reduced model (Table 1). For D2-KI rotarod testing, there was no significant effect of genotype on latency to fall (Table 1). For D2-KI rotarod testing, there were no significant interactions of genotype with age, weight, sex, and trial (Supplementary Table 1B). Separate analysis for male and female mice showed that neither sex had significant genotype effect in beam-walk or rotarod performance (Table 1).

For the Pcp2-KI cohort, there was no significant effect of genotype on average beam-walking slips (Table 1). There were no significant interactions of genotype with age, weight, beam type, side, trial, batch, or sex (Supplementary Table 1A). For Pcp2-KI rotarod testing, there were no significant interactions of genotype with age, weight, sex, and trial (Supplementary Table 1B), but there was a significant effect of genotype in the full model ($p = 0.043$). The full model was reduced to a model with no two-way interactions of genotype with other variables. The removal of these other factors resulted in only a trend-level effect of genotype in the reduced model ($p = 0.069$). However, separate analysis for each sex (see Table 1) showed that female Pcp2-KI mutant mice had improved performance with greater latency to fall ($p = 0.023$) compared to controls, but male Pcp2-KI mutants and control mice showed no difference in latency to fall ($p = 0.558$).

3.2 Region-specific differences in sensory-evoked activation in D2-KI and Pcp2-KI mice

For the D2-KI cohort, we observed a significant genotype by time-series interaction ($p = 0.005$, $\eta^2 = 0.049$) in the somatosensory cortex (Fig. 4A), where initially the BOLD activation time-series was similar between groups, but D2-KI mutant mice had a diminished response in the later sustained portion of the time-series (Fig. 4B). There were no other significant effects observed in the somatosensory cortex for D2-KI cohort. There were no significant group effects or interactions in other ROIs (data not shown).

For the Pcp2-KI cohort we observed a significant effect of genotype in the striatum ($p = 0.038$, $\eta^2 = 0.070$; Fig. 5A-B) and midbrain ($p = 0.007$, $\eta^2 = 0.115$; Fig 5C-D), with both ROIs showing lower BOLD activation in Pcp2-KI mutants compared to controls. There were no other significant main effects or interactions observed in the striatum or midbrain ROIs for the Pcp2-KI cohort. There were no significant group effects or interactions in other ROIs (data not shown).

3.3 Region-specific differences in resting-state functional connectivity in D2-KI and Pcp2-KI mice

For the D2-KI cohort we observed a significant effect of genotype on functional connectivity of the anterior medulla, such that D2-KI mutant mice showed greater functional connectivity between the anterior medulla and a 14-voxel cluster localized in the secondary

somatosensory cortex ($p_{corrected} < 0.05$; Fig. 6). We did not observe significant differences in functional connectivity for the other 11 ROIs between D2-KI mutant and control mice (data not shown).

For the Pcp2-KI cohort we observed a significant effect of genotype on functional connectivity of the striatum, such that Pcp2-KI mutant mice showed greater functional connectivity between the striatum and a 12-voxel cluster localized in the anterior medulla of the brainstem ($p_{corrected} < 0.05$; Fig. 7). We did not observe significant differences in functional connectivity for the other 11 ROIs between Pcp2-KI mutant and control mice (data not shown).

3.4 No genotype differences in diffusion MRI

For the D2-KI cohort we observed no significant effect of genotype or sex on FW in any of the 12 ROIs. There was no significant effect of genotype on FA_T for any of the 12 ROIs. We observed a significant effect of sex on FA_T in the cerebellum ($p = 0.013$) and substantia nigra ($p = 0.001$), neither of which had a significant genotype by sex interaction. Diffusion MRI statistics for the D2-KI cohort are summarized in Table 2A.

For the Pcp2-KI cohort we observed no significant effect of genotype or sex on FW in any of the 12 ROIs. There was no significant effect of genotype on FA_T for any of the 12 ROIs. We observed a significant effect of sex on FA_T in the cerebellum ($p = 0.001$), posterior medulla ($p < 0.001$), anterior medulla ($p < 0.001$), pons ($p = 0.014$), midbrain ($p = 0.007$), somatosensory cortex ($p = 0.043$) and substantia nigra ($p < 0.001$), none of which had a significant genotype by sex interaction. Diffusion MRI statistics for the D2-KI cohort are summarized in Table 2B. Although we observed no significant genotype by sex interactions in the Pcp2-KI cohort, we report those interaction p-values for the Pcp2-KI cohort in Table 1B because motor behavior in that cohort had a genotype by sex interaction.

4. Discussion

The basal ganglia and cerebellum are consistently linked to the pathophysiology and DYT1 dystonia, yet little is known about how specific torsinA dysfunction in these components contribute to abnormal network properties in the deeply interconnected sensorimotor network. In the present study, we used transgenic animal models to determine whether torsinA dysfunction caused by the *Dyt1* GAG mutation in specific cells of the basal ganglia or cerebellum would generate sensorimotor dysfunction and brain changes associated with dystonia. We evaluated motor performance with beam-walking and rotarod tasks, sensory-evoked and resting-state fMRI to assess functional activation and connectivity, and diffusion MRI (dMRI) to assess microstructure. The sensory-evoked fMRI paradigm in this study was implemented based on the framework that the somatosensory system has a major role in the pathophysiology of dystonia (Tinazzi et al., 2003), and that sensory load may reveal functional deficits to the system that are not observed at rest. We found that D2-KI mutant mice had motor deficits, abnormal sensory-evoked brain activation in the somatosensory cortex, as well as increased functional connectivity between the anterior medulla with cortex. In contrast, we found that Pcp2-KI mice had improved motor performance, reduced sensory-evoked brain activation in the striatum and midbrain,

as well as reduced functional connectivity of the striatum with the anterior medulla. We included age as a covariate in behavioral and MRI analyses, and thus our statistics do not suggest that age had a significant impact on the observed results. These findings suggest that (1) D2 cell-specific *Dyt1* GAG mediated torsinA dysfunction in the basal ganglia results in detrimental effects on the sensorimotor network and motor output, and (2) Purkinje cell-specific *Dyt1* GAG mediated torsinA dysfunction in the cerebellum results in compensatory changes in the sensorimotor network that protect against dystonia-like motor deficits.

The reduced sensory-evoked activation observed in both D2-KI and Pcp2-KI mutant mice occurred in different components of the sensorimotor network and had divergent effects on motor performance. In D2-KI mutant mice the activation deficit in the somatosensory cortex was time-dependent, such that there was no difference in the first 20s of stimulation, but signal was blunted in the latter portion of the time-series (Fig 4). Our prior work in cell-specific D2KO mice similarly showed motor deficits and blunted sensory-evoked activation in a portion of sensorimotor cortex, but was not time-dependent (Wilkes et al., 2021). Interestingly, sensory abnormalities reported in human dystonia include impaired temporal processing of sensory stimuli in dystonia patients and some non-manifesting DYT1 mutation carriers (Bradley et al., 2012; Fiorio et al., 2007; Conte et al., 2017). Our observation in D2-KI mice more closely matches this aspect of sensorimotor abnormalities seen in human dystonia than was previously observed in D2KO mice, possibly because the KI model recapitulates the GAG mutation found in early-onset primary dystonia.

The sensory-evoked activation pattern differed in Pcp2-KI mutant mice, where we found reduced activity in the striatum and midbrain over the entire 20–60s after stimulus onset. Although the cerebellum processes both sensory and motor information, these networks have complex representation and a great degree of integration at the level of the cerebellar cortex, where single regions of the cerebellar cortex may project to broad targets in the forebrain (Pisano et al., 2021). In addition, it has been demonstrated that the sensory-associated cerebellar vermis receives input from cortical motor regions in the forebrain (Coffman et al., 2011). It is possible that *Dyt1* GAG-mediated torsinA dysfunction in Purkinje cells has complex effects on motor output and sensory processing, given that the Pcp2-KI is not designed to target specific sub-populations of Purkinje neurons. This study cannot conclusively determine whether the reduced sensory-evoked activity we observed in the striatum and midbrain of Pcp2-KI mutant mice represents a true sensory processing deficit or rather compensatory changes to the system. Given that there was no significant motor deficit in Pcp2-KI mutant mice as a whole, which entails a great degree of sensorimotor integration, we do not believe our neuroimaging findings to represent a sensory processing deficit in Pcp2-KI mutant mice. It is interesting that while male Pcp2-KI mice showed no deficit compared to male controls, female Pcp2-KI mutant mice showed improved rotarod performance over female controls, possibly representing an interaction of the *Dyt1* GAG mutation with estrogen in modulating glutamatergic signaling in the cerebellum (Hedges et al., 2012). One interpretation of our neuroimaging findings is that sensory domain cortico-striatal projections have reduced gain. Indeed, long-term depression (LTD) of corticostriatal projections was found in mice with whole-brain *Dyt1* GAG KI (Dang et al., 2012) and LTD has been associated with reduced BOLD activity in

fMRI (Rottmann et al., 2010). Although we observed no sex differences on neuroimaging measures, there is evidence from human neuroimaging studies of sex differences in the cerebellum, particularly the vermis (Raz et al., 2001).

Analyses of resting-state functional connectivity provided information about the sensorimotor network without a sensory load. In D2-KI mutant mice there was greater functional connectivity between the anterior medulla and a portion of the secondary somatosensory cortex. In Pcp2-KI mutant mice there was greater functional connectivity between the striatum and anterior medulla. Prior work in whole-brain *Dyt1* ΔGAG KI similarly showed altered functional connectivity of the striatum (DeSimone et al., 2016), which has also been observed in patients with DYT1 dystonia (Mazere et al., 2021). Moreover, resting-state functional connectivity deficits in the sensorimotor network were observed in clinically manifesting DYT1 mutation carriers, but were absent in non-manifesting mutation carriers (Premi et al., 2016). It is important to note that basal ganglia and cerebellar networks were not compared by Premi et al., (2016), as methodological limitations prevented construction of common subcortical networks across patients.

Structural alterations to the basal ganglia, cerebellum, and other components of the sensorimotor network have been reported in human dystonia (see MacIver et al., 2022). Microstructural differences have also been reported in the basal ganglia and cerebellum in *Dyt1* ΔGAG KI mice (DeSimone et al., 2016; Song et al., 2014, 2013; Uluğ et al., 2011). The D2-KI and Pcp2-KI models utilized in this study are cell-specific versions of the *Dyt1* ΔGAG KI mouse model. However, this study did not find microstructural changes in either D2-KI or Pcp2-KI mutant mice. Previous work has reported lower FA in the striatum of *Dyt1* KI mice (Uluğ et al., 2011), and *Dyt1* KO mice had lower FA in the sensorimotor cortex and brainstem (Vo et al., 2015a). It is important to note that both of those investigations were performed using *ex vivo* methods for dMRI, which permits long scan times and higher spatial resolution than is possible *in vivo*. It may be that we did not detect microstructural changes in D2-KI and Pcp2-KI models because they occur on a smaller scale than our paradigm was sensitive to. For *in vivo* dMRI in this study slice thickness was set to 0.7 mm (700 μm) in order to achieve feasible scan times and acceptable signal-to-noise ratio, compared to the 0.0625 mm (62.5 μm) isotropic voxel size used for *ex vivo* dMRI by Uluğ et al. (2011) and Vo et al. (2015a). Most methodologically similar to the present study, DeSimone et al. (2016) performed *in vivo* dMRI in *Dyt1* KI mice and reported increased free-water in the striatum and cerebellum. All three of these papers that reported microstructural differences were performed in the *Dyt1* KI model, where the whole brain was affected by torsinA mutation. It may be that microstructure is more impacted when torsinA dysfunction occurs throughout the brain, rather than in specific neuronal populations.

In the D2-KI model, targeted cell types were medium spiny neurons of the indirect pathway, striatal cholinergic interneurons, and dopaminergic neurons of the basal ganglia. D2-KI mutant mice showed motor performance deficits and impaired sensory-evoked activation in the somatosensory cortex. These observations could represent impaired thalamocortical output from the basal ganglia. Supporting this notion, neuroimaging in human dystonia revealed impaired thalamocortical connectivity that was mediated by phenotypic variability,

whereas corticostriatal and corticospinal pathways were not different between groups (Vo et al., 2015b). Our D2-KI resting-state functional connectivity findings also fit in this framework: deficient thalamocortical output from the basal ganglia could result in a compensatory change where signals between the cortex and medulla are amplified to overcome for the low gain of thalamocortical relays.

In contrast, there were no motor deficits in Pcp2-KI mutants, and we observed improved motor performance in female Pcp2-KI mutants. This finding is novel but matches our hypothesis based on prior work in the Purkinje cell-specific *Dyt1* KO model (Yokoi et al., 2012; Zhang et al., 2011). In the Pcp2-KI model, *Dyt1* GAG mutation is restricted to cerebellar Purkinje cells, and the cerebellum (particularly Purkinje cells) shows a greater degree of sexual dimorphism than many other areas of the brain (Abel et al., 2011; Raz et al., 2001); this may partially explain the improved performance in female Pcp2-KI mutants, but no differences in males. We also observed reduced sensory-evoked activation in the striatum and midbrain of Pcp2-KI mutant mice, along with increased functional connectivity between the striatum and medulla. It is possible that the observed effects on motor behavior are mediated by reduced Purkinje cell output to the dentate nucleus. In support of this interpretation, electrophysiological recordings from the cerebellum of *Dyt1* KI mice showed non-tonically firing Purkinje cells had lower peak frequency, more pauses between bursting activity, and higher coefficient of variation compared to control mice (Liu et al., 2020). Another study that knocked down torsinA expression in adult wild-type mice also reported decreased firing rate of cerebellar Purkinje cells, but their manipulation induced dystonic symptoms (Fremont et al., 2017). These different outcomes in relation to a similar reduction of Purkinje cell firing may be explained by the presence of GAG mutant torsinA throughout development, as the same manipulation in juvenile animals failed to induce dystonic symptoms, or by unintended effects of the shRNA knockdown approach in adult animals that do not naturally occur in DYT1 genetic dystonia. In human DYT1 dystonia, structural neuroimaging differences in the cerebellothalamic tract were reported to distinguish nonmanifesting and clinically manifesting DYT1 mutation carriers — both groups showed alterations in a portion of the cerebellothalamic tract proximal to the cerebellum, but nonmanifesting carriers showed an additional compensatory alteration in a distal portion of the cerebellothalamic tract (Argyelan et al., 2009). In cervical dystonia, repetitive transcranial magnetic stimulation (rTMS) to the cerebellum, using a stimulation paradigm designed to reduce firing of underlying neuronal populations, was found to improve motor symptoms (Koch et al., 2014). Although we observed differences in areas other than the cerebellum itself, the cited studies provide a possible mechanism to interpret the finding of improved motor behavior in Pcp2-KI mice: modified cerebellar output might exert protective effects on sensorimotor circuitry against dystonic motor symptoms. It remains unclear whether the observed effects on motor behavior and sensory-evoked fMRI in Pcp2-KI mice were mediated by shared or distinct mechanisms.

Investigating cell-specific torsinA dysfunction is crucial for understanding the complex network of pathophysiology in DYT1 dystonia. Considered together, our findings in the D2-KI and Pcp2-KI strains can help to elucidate components of the sensorimotor circuit which may be sensitive to effects of GAG mutant torsinA. Prior evidence does not suggest there is impairment of the ascending sensory pathway from the spinal cord to somatosensory

cortex in dystonia (Conte et al., 2019). In the present study, it is interesting that atypical activation and connectivity patterns in both mouse models did not occur in the targeted brain area, but rather in downstream components of the sensorimotor network — lending further support to the conceptualization of dystonia as a network disorder (Simonyan, 2018). The importance of the cerebellum in dystonia has become more widely appreciated, yet recent focus has shifted to possible therapeutic effects achieved by targeting the cerebellum or its outputs to the thalamus (Chen et al., 2014; Tewari et al., 2017). This study's findings make an impactful contribution toward our understanding of neurological mechanisms mediating motor outcomes in DYT1 dystonia and may inform future research toward a cure.

Supplementary Material

Refer to Web version on PubMed Central for supplementary material.

Acknowledgements

References

Abel JM, Witt DM, Rissman EF, 2011. Sex differences in the cerebellum and frontal cortex: roles of estrogen receptor alpha and sex chromosome genes. Neuroendocrinology 93, 230–240. 10.1159/000324402 [PubMed: 21325792]

Albanese A, Bhatia K, Bressman SB, DeLong MR, Fahn S, Fung VSC, Hallett M, Jankovic J, Jinnah HA, Klein C, Lang AE, Mink JW, Teller JK, 2013. Phenomenology and classification of dystonia: A consensus update: Dystonia: Phenomenology and classification. Movement Disorders 28, 863–873. 10.1002/mds.25475 [PubMed: 23649720]

Argyelan Miklos, Carbon M, Niethammer M, Ulug AM, Voss HU, Bressman SB, Dhawan V, Eidelberg D, 2009. Cerebellothalamocortical connectivity regulates penetrance in dystonia. J Neurosci 29, 9740–9747. 10.1523/JNEUROSCI.2300-09.2009 [PubMed: 19657027]

Argyelan M, Carbon M, Niethammer M, Ulug AM, Voss HU, Bressman SB, Dhawan V, Eidelberg D, 2009. Cerebellothalamocortical Connectivity Regulates Penetrance in Dystonia. Journal of Neuroscience 29, 9740–9747. 10.1523/JNEUROSCI.2300-09.2009 [PubMed: 19657027]

Avants BB, Yushkevich P, Pluta J, Minkoff D, Korczykowski M, Detre J, Gee JC, 2010. The optimal template effect in hippocampus studies of diseased populations. Neuroimage 49, 2457–2466. 10.1016/j.neuroimage.2009.09.062 [PubMed: 19818860]

Bosshard SC, Stuker F, von Deuster C, Schroeter A, Rudin M, 2015. BOLD fMRI of C-Fiber Mediated Nociceptive Processing in Mouse Brain in Response to Thermal Stimulation of the Forepaws. PLoS One 10, e0126513. 10.1371/journal.pone.0126513

Bradley D, Whelan R, Kimmich O, O'Riordan S, Mulrooney N, Brady P, Walsh R, Reilly RB, Hutchinson S, Molloy F, Hutchinson M, 2012. Temporal discrimination thresholds in adult-onset primary torsion dystonia: an analysis by task type and by dystonia phenotype. J Neurol 259, 77–82. 10.1007/s00415-011-6125-7 [PubMed: 21656045]

Burciu RG, Hess CW, Coombes SA, Ofori E, Shukla P, Chung JW, McFarland NR, Wagle Shukla A, Okun MS, Vaillancourt DE, 2017. Functional activity of the sensorimotor cortex and cerebellum

relates to cervical dystonia symptoms. Hum Brain Mapp 38, 4563–4573. 10.1002/hbm.23684 [PubMed: 28594097]

Burke RE, Fahn S, Marsden CD, 1986. Torsion dystonia: a double-blind, prospective trial of high-dosage trihexyphenidyl. Neurology 36, 160–164. 10.1212/wnl.36.2.160 [PubMed: 3511401]

Carbon M, Kingsley PB, Tang C, Bressman S, Eidelberg D, 2008. Microstructural white matter changes in primary torsion dystonia. Mov Disord 23, 234–239. 10.1002/mds.21806 [PubMed: 17999428]

Chen CH, Fremont R, Arteaga-Bracho EE, Khodakhah K, 2014. Short latency cerebellar modulation of the basal ganglia. Nature Neuroscience 17, 1767–1775. 10.1038/nn.3868 [PubMed: 25402853]

Chu WT, DeSimone JC, Riffe CJ, Liu H, Chakrabarty P, Giasson BI, Vedam-Mai V, Vaillancourt DE, 2020. Alpha-synuclein induces progressive changes in brain microstructure and sensory-evoked brain function that precedes locomotor decline. J. Neurosci. 10.1523/JNEUROSCI.0189-20.2020

Coffman KA, Dum RP, Strick PL, 2011. Cerebellar vermis is a target of projections from the motor areas in the cerebral cortex. Proc Natl Acad Sci U S A 108, 16068–16073. 10.1073/pnas.1107904108

Colon-Perez LM, Ibanez KR, Suarez M, Torroella K, Acuna K, Ofori E, Levites Y, Vaillancourt DE, Golde TE, Chakrabarty P, Febo M, 2019. Neurite orientation dispersion and density imaging reveals white matter and hippocampal microstructure changes produced by Interleukin-6 in the TgCRND8 mouse model of amyloidosis. Neuroimage 202, 116138. 10.1016/j.neuroimage.2019.116138

Conte A, Defazio G, Hallett M, Fabbrini G, Berardelli A, 2019. The role of sensory information in the pathophysiology of focal dystonias. Nat Rev Neurol 15, 224–233. 10.1038/s41582-019-0137-9 [PubMed: 30700825]

Conte A, McGovern EM, Narasimham S, Beck R, Killian O, O'Riordan S, Reilly RB, Hutchinson M, 2017. Temporal Discrimination: Mechanisms and Relevance to Adult-Onset Dystonia. Front Neurol 8, 625. 10.3389/fneur.2017.00625 [PubMed: 29234300]

Cox RW, 1996. AFNI: software for analysis and visualization of functional magnetic resonance neuroimages. Comput. Biomed. Res. 29, 162–173. 10.1006/cbmr.1996.0014 [PubMed: 8812068]

Cox RW, Chen G, Glen DR, Reynolds RC, Taylor PA, 2017. fMRI clustering and false-positive rates. Proc Natl Acad Sci U S A 114, E3370–E3371. 10.1073/pnas.1614961114

Dang MT, Yokoi F, Cheetham CC, Lu J, Vo V, Lovinger DM, Li Y, 2012. An anticholinergic reverses motor control and corticostriatal LTD deficits in Dyt1 ΔGAG knock-in mice. Behavioural Brain Research 226, 465–472. 10.1016/j.bbr.2011.10.002 [PubMed: 21995941]

Dang MT, Yokoi F, McNaught K. St P, Jengelley T-A, Jackson T, Li J, Li Y, 2005. Generation and characterization of Dyt1 ΔGAG knock-in mouse as a model for early-onset dystonia. Experimental Neurology 196, 452–463. 10.1016/j.expneurol.2005.08.025 [PubMed: 16242683]

DeAndrade MP, Trongnetrpunya A, Yokoi F, Cheetham CC, Peng N, Wyss JM, Ding M, Li Y, 2016. Electromyographic evidence in support of a knock-in mouse model of DYT1 Dystonia: EMG of a DYT1 Dystonia Mouse. Movement Disorders 31, 1633–1639. 10.1002/mds.26677 [PubMed: 27241685]

DeSimone JC, Febo M, Shukla P, Ofori E, Colon-Perez LM, Li Y, Vaillancourt DE, 2016. In vivo imaging reveals impaired connectivity across cortical and subcortical networks in a mouse model of DYT1 dystonia. Neurobiol. Dis. 95, 35–45. 10.1016/j.nbd.2016.07.005 [PubMed: 27404940]

DeSimone JC, Pappas SS, Febo M, Burciu RG, Shukla P, Colon-Perez LM, Dauer WT, Vaillancourt DE, 2017. Forebrain knock-out of torsinA reduces striatal free-water and impairs whole-brain functional connectivity in a symptomatic mouse model of DYT1 dystonia. Neurobiol. Dis. 106, 124–132. 10.1016/j.nbd.2017.06.015 [PubMed: 28673740]

Fahn S, 1983. High dosage anticholinergic therapy in dystonia. Neurology 33, 1255–1261. 10.1212/wnl.33.10.1255 [PubMed: 6136938]

Fiorio M, Gambarin M, Valente EM, Liberini P, Loi M, Cossu G, Moretto G, Bhatia KP, Defazio G, Aglioti SM, Fiaschi A, Tinazzi M, 2007. Defective temporal processing of sensory stimuli in DYT1 mutation carriers: a new endophenotype of dystonia? Brain 130, 134–142. 10.1093/brain/awl283 [PubMed: 17105745]

Fremont R, Tewari A, Angueyra C, Khodakhah K, 2017. A role for cerebellum in the hereditary dystonia DYT1. eLife 6. 10.7554/eLife.22775

Garyfallidis E, Brett M, Amirbekian B, Rokem A, van der Walt S, Descoteaux M, Nimmo-Smith I, Dipy Contributors, 2014. Dipy, a library for the analysis of diffusion MRI data. Front Neuroinform 8, 8. 10.3389/fninf.2014.00008 [PubMed: 24600385]

Gong S, Doughty M, Harbaugh CR, Cummins A, Hatten ME, Heintz N, Gerfen CR, 2007. Targeting Cre recombinase to specific neuron populations with bacterial artificial chromosome constructs. J. Neurosci. 27, 9817–9823. 10.1523/JNEUROSCI.2707-07.2007 [PubMed: 17855595]

Hallett M, 1995. Is dystonia a sensory disorder? Ann. Neurol. 38, 139–140. 10.1002/ana.410380203 [PubMed: 7654059]

Hayashi M, Nagao Y, Kimura K, Hachimori K, Nomura Y, Segawa M, 2008. [Case of DYT1 dystonia (early-onset torsion dystonia) showing long-term focal dystonia in the arm]. No To Hattatsu 40, 483–486. [PubMed: 19039992]

Hedges VL, Ebner TJ, Meisel RL, Mermelstein PG, 2012. The cerebellum as a target for estrogen action. Front Neuroendocrinol 33, 403–411. 10.1016/j.yfrne.2012.08.005 [PubMed: 22975197]

Jenkinson M, Beckmann CF, Behrens TEJ, Woolrich MW, Smith SM, 2012. FSL. Neuroimage 62, 782–790. 10.1016/j.neuroimage.2011.09.015 [PubMed: 21979382]

Kim J, Yao A, Atherley R, Carstens E, Jinks SL, Antognini JF, 2007. Neurons in the ventral spinal cord are more depressed by isoflurane, halothane, and propofol than are neurons in the dorsal spinal cord. Anesth. Analg. 105, 1020–1026, table of contents. 10.1213/01.ane.0000280483.17854.56 [PubMed: 17898382]

Koch G, Porcacchia P, Ponzo V, Carrillo F, Cáceres-Redondo MT, Brusa L, Desiato MT, Arciprete F, Di Lorenzo F, Pisani A, Caltagirone C, Palomar FJ, Mir P, 2014. Effects of two weeks of cerebellar theta burst stimulation in cervical dystonia patients. Brain Stimul 7, 564–572. 10.1016/j.brs.2014.05.002 [PubMed: 24881805]

Lee A, Furuya S, Altenmüller E, 2014. Epidemiology and treatment of 23 musicians with task specific tremor. J Clin Mov Disord 1, 5. 10.1186/2054-7072-1-5 [PubMed: 26788331]

Liu Y, Xing H, Wilkes BJ, Yokoi F, Chen H, Vaillancourt DE, Li Y, 2020. The abnormal firing of Purkinje cells in the knockin mouse model of DYT1 dystonia. Brain Res Bull 165, 14–22. 10.1016/j.brainresbull.2020.09.011 [PubMed: 32976982]

Lyu S, Xing H, DeAndrade MP, Perez PD, Yokoi F, Febo M, Walters AS, Li Y, 2020. The Role of BTBD9 in the Cerebellum, Sleep-like Behaviors and the Restless Legs Syndrome. Neuroscience 440, 85–96. 10.1016/j.neuroscience.2020.05.021 [PubMed: 32446853]

MacIver CL, Tax CMW, Jones DK, Peall KJ, 2022. Structural magnetic resonance imaging in dystonia: A systematic review of methodological approaches and findings. Eur J Neurol 29, 3418–3448. 10.1111/ene.15483 [PubMed: 35785410]

Maltese M, Martella G, Madeo G, Fagiolo I, Tassone A, Ponterio G, Sciamanna G, Burbaud P, Conn PJ, Bonsi P, Pisani A, 2014. Anticholinergic drugs rescue synaptic plasticity in DYT1 dystonia: role of M1 muscarinic receptors. Mov Disord 29, 1655–1665. 10.1002/mds.26009 [PubMed: 25195914]

Martella G, Maltese M, Nisticò R, Schirinzi T, Madeo G, Sciamanna G, Ponterio G, Tassone A, Mandolesi G, Vanni V, Pignatelli M, Bonsi P, Pisani A, 2014. Regional specificity of synaptic plasticity deficits in a knock-in mouse model of DYT1 dystonia. Neurobiol. Dis. 65, 124–132. 10.1016/j.nbd.2014.01.016 [PubMed: 24503369]

Martella G, Tassone A, Sciamanna G, Platania P, Cuomo D, Viscomi MT, Bonsi P, Cacci E, Biagioni S, Usiello A, Bernardi G, Sharma N, Standaert DG, Pisani A, 2009. Impairment of bidirectional synaptic plasticity in the striatum of a mouse model of DYT1 dystonia: role of endogenous acetylcholine. Brain 132, 2336–2349. 10.1093/brain/awp194 [PubMed: 19641103]

Mazere J, Dilharreguy B, Catheline G, Vidailhet M, Deffains M, Vimont D, Ribot B, Barse E, Cif L, Mazoyer B, Langbour N, Pisani A, Allard M, Lamare F, Guehl D, Fernandez P, Burbaud P, 2021. Striatal and cerebellar vesicular acetylcholine transporter expression is disrupted in human DYT1 dystonia. Brain 144, 909–923. 10.1093/brain/awaa465 [PubMed: 33638639]

Meoni S, Macerollo A, Moro E, 2020. Sex differences in movement disorders. Nat Rev Neurol 16, 84–96. 10.1038/s41582-019-0294-x [PubMed: 31900464]

Miyazaki Y, 2012. Efficacy of zolpidem for dystonia: a study among different subtypes. Front. Neur. 6. 10.3389/fneur.2012.00058

Ozelius LJ, Hewett JW, Page CE, Bressman SB, Kramer PL, Shalish C, de Leon D, Brin MF, Raymond D, Corey DP, Fahn S, Risch NJ, Buckler AJ, Gusella JF, Breakefield XO, 1997. The early-onset torsion dystonia gene (DYT1) encodes an ATP-binding protein. Nature Genetics 17, 40–48. 10.1038/ng0997-40 [PubMed: 9288096]

Pisano TJ, Dhanerawala ZM, Kislin M, Bakshinskaya D, Engel EA, Hansen EJ, Hoag AT, Lee J, de Oude NL, Venkataraju KU, Verpeut JL, Hoebeek FE, Richardson BD, Boele H-J, Wang SS-H, 2021. Homologous organization of cerebellar pathways to sensory, motor, and associative forebrain. Cell Rep 36, 109721. 10.1016/j.celrep.2021.109721

Premi E, Diano M, Gazzina S, Cauda F, Gualeni V, Tinazzi M, Fiorio M, Liberini P, Lazzarini C, Archetti S, Biasiotto G, Turla M, Bertasi V, Cotelli M, Gasparotti R, Padovani A, Borroni B, 2016. Functional Connectivity Networks in Asymptomatic and Symptomatic DYT1 Carriers. Mov Disord 31, 1739–1743. 10.1002/mds.26725 [PubMed: 27453152]

Quartarone A, Hallett M, 2013. Emerging concepts in the physiological basis of dystonia. Mov. Disord. 28, 958–967. 10.1002/mds.25532 [PubMed: 23893452]

Raz N, Gunning-Dixon F, Head D, Williamson A, Acker JD, 2001. Age and sex differences in the cerebellum and the ventral pons: a prospective MR study of healthy adults. AJNR Am J Neuroradiol 22, 1161–1167. [PubMed: 11415913]

Rijpkema M, Everaerd D, van der Pol C, Franke B, Tendolkar I, Fernández G, 2012. Normal sexual dimorphism in the human basal ganglia. Hum Brain Mapp 33, 1246–1252. 10.1002/hbm.21283 [PubMed: 21523857]

Rottmann S, Jung K, Vohn R, Ellrich J, 2010. Long-term depression of pain-related cerebral activation in healthy man: an fMRI study. Eur J Pain 14, 615–624. 10.1016/j.ejpain.2009.10.006 [PubMed: 19896873]

Saad ZS, Chen G, Reynolds RC, Christidis PP, Hammett KR, Bellgowan PSF, Cox RW, 2006. Functional imaging analysis contest (FIAC) analysis according to AFNI and SUMA. Hum Brain Mapp 27, 417–424. 10.1002/hbm.20247 [PubMed: 16568421]

Satterthwaite TD, Elliott MA, Gerraty RT, Ruparel K, Loughead J, Calkins ME, Eickhoff SB, Hakonarson H, Gur RC, Gur RE, Wolf DH, 2013. An improved framework for confound regression and filtering for control of motion artifact in the preprocessing of resting-state functional connectivity data. Neuroimage 64, 240–256. 10.1016/j.neuroimage.2012.08.052 [PubMed: 22926292]

Scuteri D, Rombolà L, Natoli S, Pisani A, Bonsi P, Hamamura K, Bagetta G, Tonin P, Corasaniti MT, 2021. Exploitation of Thermal Sensitivity and Hyperalgesia in a Mouse Model of Dystonia. Life (Basel) 11, 985. 10.3390/life11090985 [PubMed: 34575134]

Sharma N, Baxter MG, Petravicz J, Bragg DC, Schienda A, Standaert DG, Breakefield XO, 2005. Impaired motor learning in mice expressing torsinA with the DYT1 dystonia mutation. J Neurosci 25, 5351–5355. 10.1523/JNEUROSCI.0855-05.2005 [PubMed: 15930383]

Shashidharan P, Sandu D, Potla U, Armata IA, Walker RH, McNaught KS, Weisz D, Sreenath T, Brin MF, Olanow CW, 2005. Transgenic mouse model of early-onset DYT1 dystonia. Hum Mol Genet 14, 125–133. 10.1093/hmg/ddi012 [PubMed: 15548549]

Simonyan K, 2018. Neuroimaging Applications in Dystonia. Int. Rev. Neurobiol. 143, 1–30. 10.1016/bs.irn.2018.09.007 [PubMed: 30473192]

Song C-H, Bernhard D, Bolarinwa C, Hess EJ, Smith Y, Jinnah HA, 2013. Subtle microstructural changes of the striatum in a DYT1 knock-in mouse model of dystonia. Neurobiol Dis 54, 362–371. 10.1016/j.nbd.2013.01.008 [PubMed: 23336980]

Song C-H, Bernhard D, Hess EJ, Jinnah HA, 2014. Subtle microstructural changes of the cerebellum in a knock-in mouse model of DYT1 dystonia. Neurobiology of Disease 62, 372–380. 10.1016/j.nbd.2013.10.003 [PubMed: 24121114]

Suttrup I, Oberdiek D, Suttrup J, Osada N, Evers S, Marziniak M, 2011. Loss of sensory function in patients with idiopathic hand dystonia. Mov Disord 26, 107–113. 10.1002/mds.23425 [PubMed: 20960475]

Tewari A, Fremont R, Khodakhah K, 2017. It's not just the basal ganglia: Cerebellum as a target for dystonia therapeutics. Mov. Disord. 32, 1537–1545. 10.1002/mds.27123 [PubMed: 28843013]

Tinazzi M, Rosso T, Fiaschi A, 2003. Role of the somatosensory system in primary dystonia. Mov. Disord. 18, 605–622. 10.1002/mds.10398 [PubMed: 12784263]

Ulu AM, Vo A, Argyelan M, Tanabe L, Schiffer WK, Dewey S, Dauer WT, Eidelberg D, 2011. Cerebellothalamocortical pathway abnormalities in torsinA DYT1 knock-in mice. Proc. Natl. Acad. Sci. U.S.A. 108, 6638–6643. 10.1073/pnas.1016445108 [PubMed: 21464304]

Vo A, Sako W, Dewey SL, Eidelberg D, Ulu AM, 2015a. 18FDG-microPET and MR DTI findings in Tor1a+/− heterozygous knock-out mice. Neurobiol. Dis. 73, 399–406. 10.1016/j.nbd.2014.10.020 [PubMed: 25447231]

Vo A, Sako W, Niethammer M, Carbon M, Bressman SB, Ulu AM, Eidelberg D, 2015b. Thalamocortical Connectivity Correlates with Phenotypic Variability in Dystonia. Cereb Cortex 25, 3086–3094. 10.1093/cercor/bhu104 [PubMed: 24860017]

Wilkes BJ, DeSimone JC, Liu Y, Chu WT, Coombes SA, Li Y, Vaillancourt DE, 2021. Cell-specific effects of Dyt1 knock-out on sensory processing, network-level connectivity, and motor deficits. Exp Neurol 343, 113783. 10.1016/j.expneurol.2021.113783

Xing H, Yokoi F, Walker AL, Torres-Medina R, Liu Y, Li Y, 2022. Electrophysiological characterization of the striatal cholinergic interneurons in Dyt1 GAG knock-in mice. Dystonia 1, 10557. 10.3389/dyst.2022.10557

Yokoi F, Dang MT, Li Y, 2012. Improved motor performance in Dyt1 GAG heterozygous knock-in mice by cerebellar Purkinje-cell specific Dyt1 conditional knocking-out. Behav. Brain Res. 230, 389–398. 10.1016/j.bbr.2012.02.029 [PubMed: 22391119]

Yokoi F, Oleas J, Xing H, Liu Y, Dexter KM, Misztal C, Gerard M, Efimenko I, Lynch P, Villanueva M, Alsina R, Krishnaswamy S, Vaillancourt DE, Li Y, 2020. Decreased number of striatal cholinergic interneurons and motor deficits in dopamine receptor 2-expressing-cell-specific Dyt1 conditional knockout mice. Neurobiol. Dis. 134, 104638. 10.1016/j.nbd.2019.104638

Zhang L, Yokoi F, Jin Y-H, DeAndrade MP, Hashimoto K, Standaert DG, Li Y, 2011. Altered dendritic morphology of Purkinje cells in Dyt1 GAG knock-in and purkinje cell-specific Dyt1 conditional knockout mice. PLoS ONE 6, e18357. 10.1371/journal.pone.0018357

Highlights

- *Dyt1* GAG knock-in has differential effects in the basal ganglia and cerebellum

- Dopamine-2 receptor specific *Dyt1* knock-in mice display motor deficits

- Purkinje neuron specific *Dyt1* knock-in mice have improved motor performance

- D2-KI and Pcp2-KI mice have unique sensorimotor activation and network connectivity
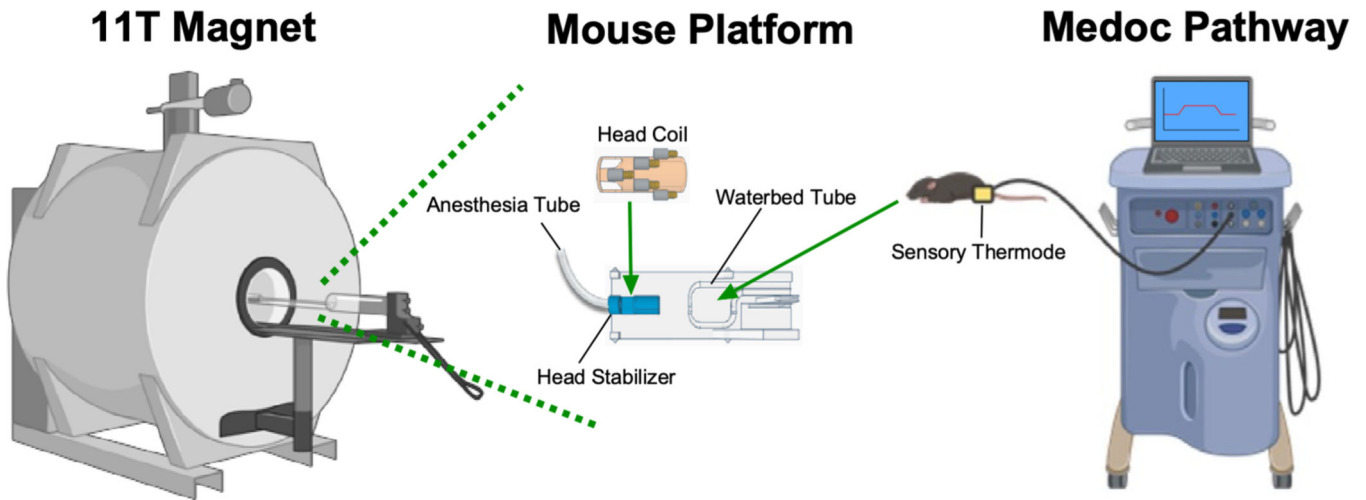
Figure 1. Imaging setup.

Imaging was performed on an 11.1 Tesla MRI scanner with a Magnex Scientific 40 cm horizontal magnet (Bruker BioSpin, Billerica, MA). For imaging, animals were placed on a custom-designed mouse platform, which included anesthesia provided through a head stabilizer with a surface transmit/receive radiofrequency head coil. Core body temperature was maintained during imaging with a heated waterbed tube placed underneath the animal. A Medoc PATHWAY heating thermode was placed on the right hindlimb of the animal and controlled by an associated computer setup.
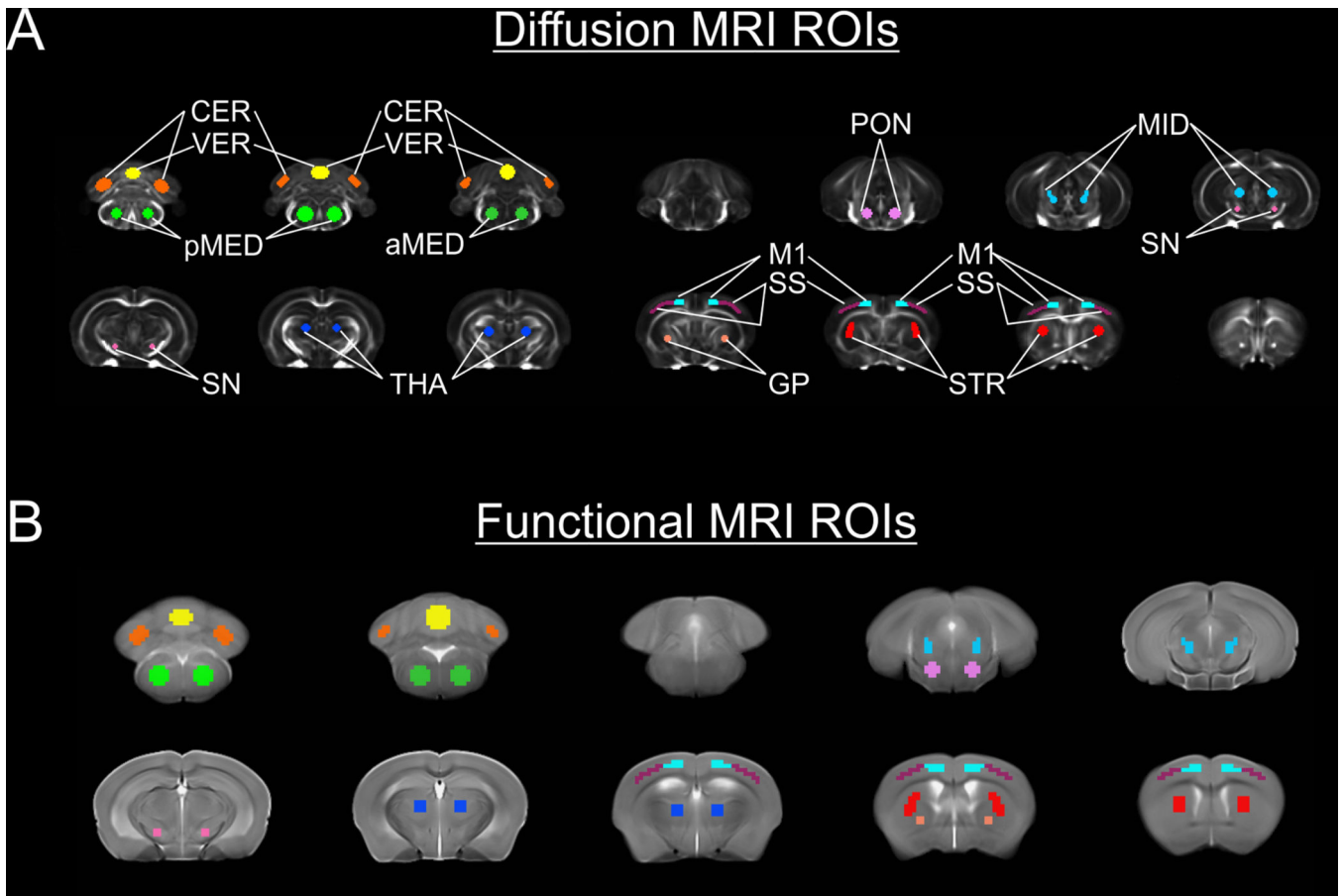
Figure 2. Regions of Interest.
The top panel (A) shows diffusion MRI regions of interest overlaid on top of the fractional anisotropy template image: cerebellum (CER; orange), vermis (VER; yellow), posterior medulla (pMED; light green), anterior medulla (aMED; dark green), pons (PON; pink), midbrain (MID; turquoise), substantia nigra (SN; magenta), thalamus (THA; dark blue), globus pallidus (GP; orange), somatosensory cortex (SS; purple), primary motor cortex (M1; light blue), and striatum (STR; red).
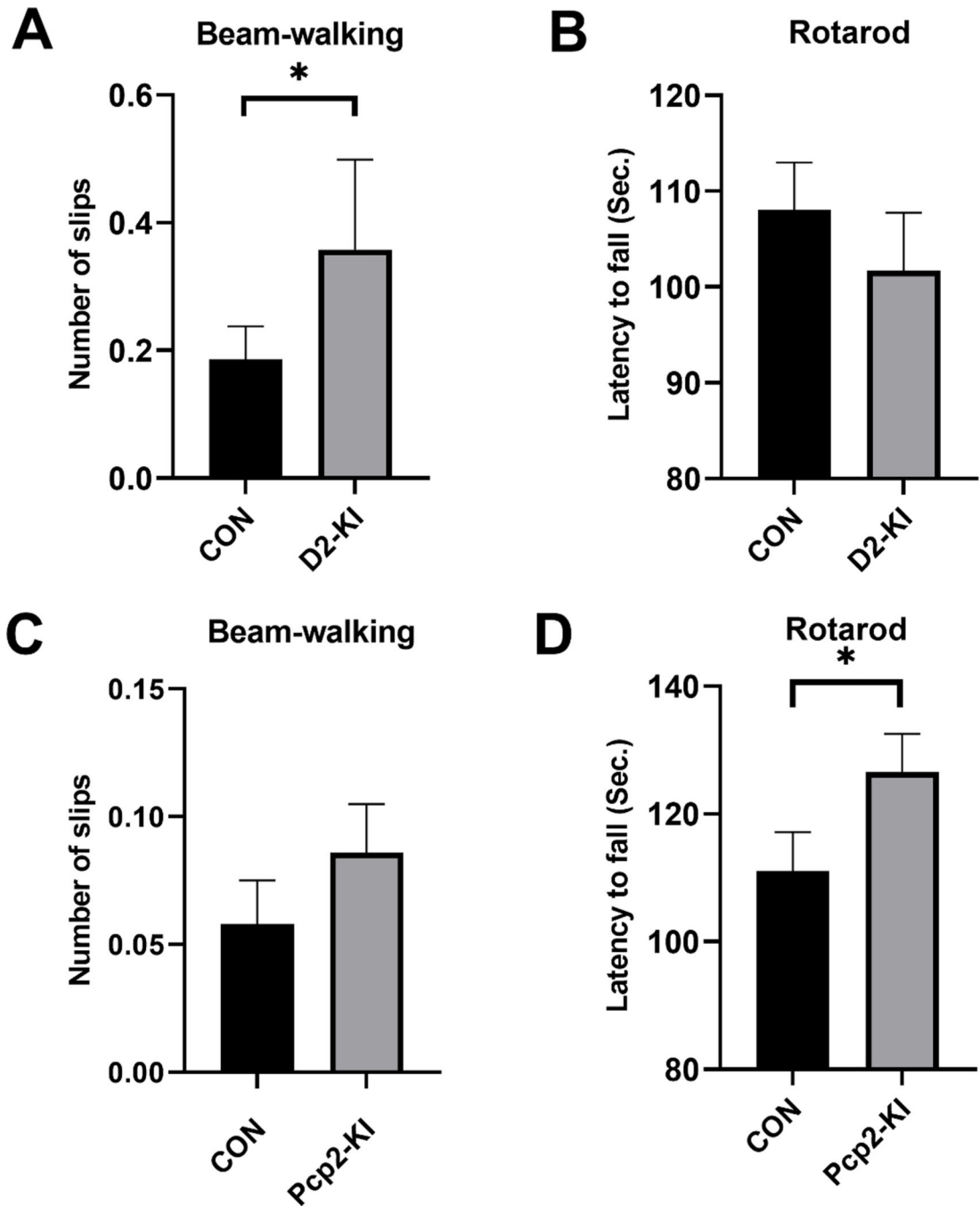
Figure 3. Motor performance in D2-KI and Pcp2-KI mice.

In the D2-KI cohort, mutant mice displayed a significant (*$p < 0.05$, reduced model) beam-walking deficit (A), but no difference in rotarod performance (B). In contrast, Pcp2-KI mutant mice showed no difference in beam-walking performance (C), but significantly improved performance (*$p < 0.05$ in the full model, $p = 0.069$ in the reduced model) on the rotarod (D). Data are shown as the mean number of slips for beam-walking and the mean latency to fall for rotarod (error bars: SEM).
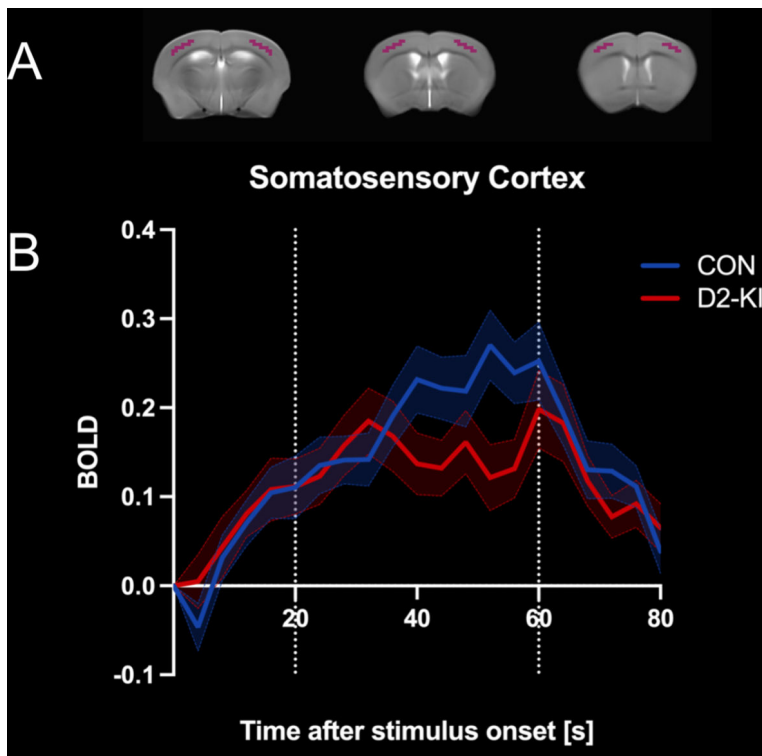
Figure 4. D2-KI sensory-evoked BOLD.
(A) The somatosensory cortex region of interest overlaid on top of mouse anatomical template image. (B) Blood oxygen level dependent (BOLD) percent signal change in the somatosensory cortex as a result of the sensory-evoked fMRI paradigm. There was a significant interaction between genotype and time-course, such that D2-KI mice (red) had blunted BOLD signal during the latter portion of sustained stimulus compared to controls (blue).
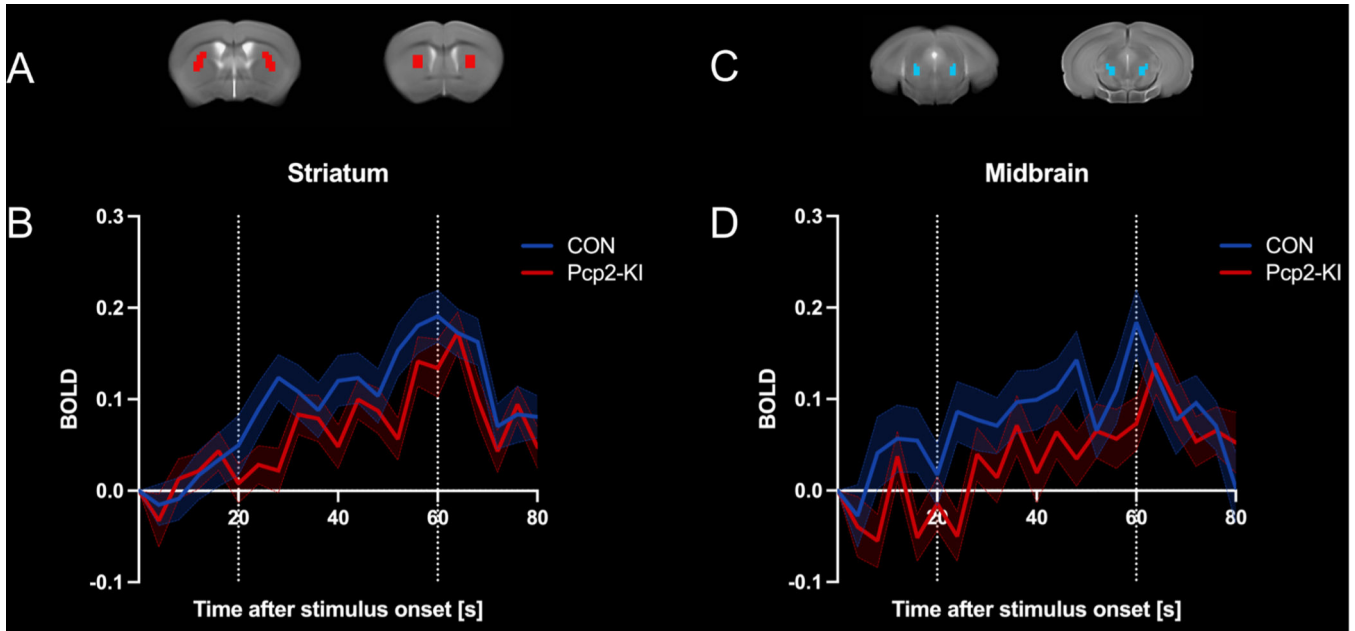
Figure 5. Pcp2-KI sensory-evoked BOLD.
The top panel shows regions of interest for the striatum (A) and midbrain (B) regions of interest overlaid on top of the mouse anatomical template image. The bottom panel shows sensory-evoked blood oxygen level dependent (BOLD) percent signal change in the striatum (C) and midbrain (D), which showed a significant effect of genotype such that Pcp2-KI mice (red) had lower BOLD signal during 20–60 period after stimulus onset compared to controls (blue) in both brain regions.
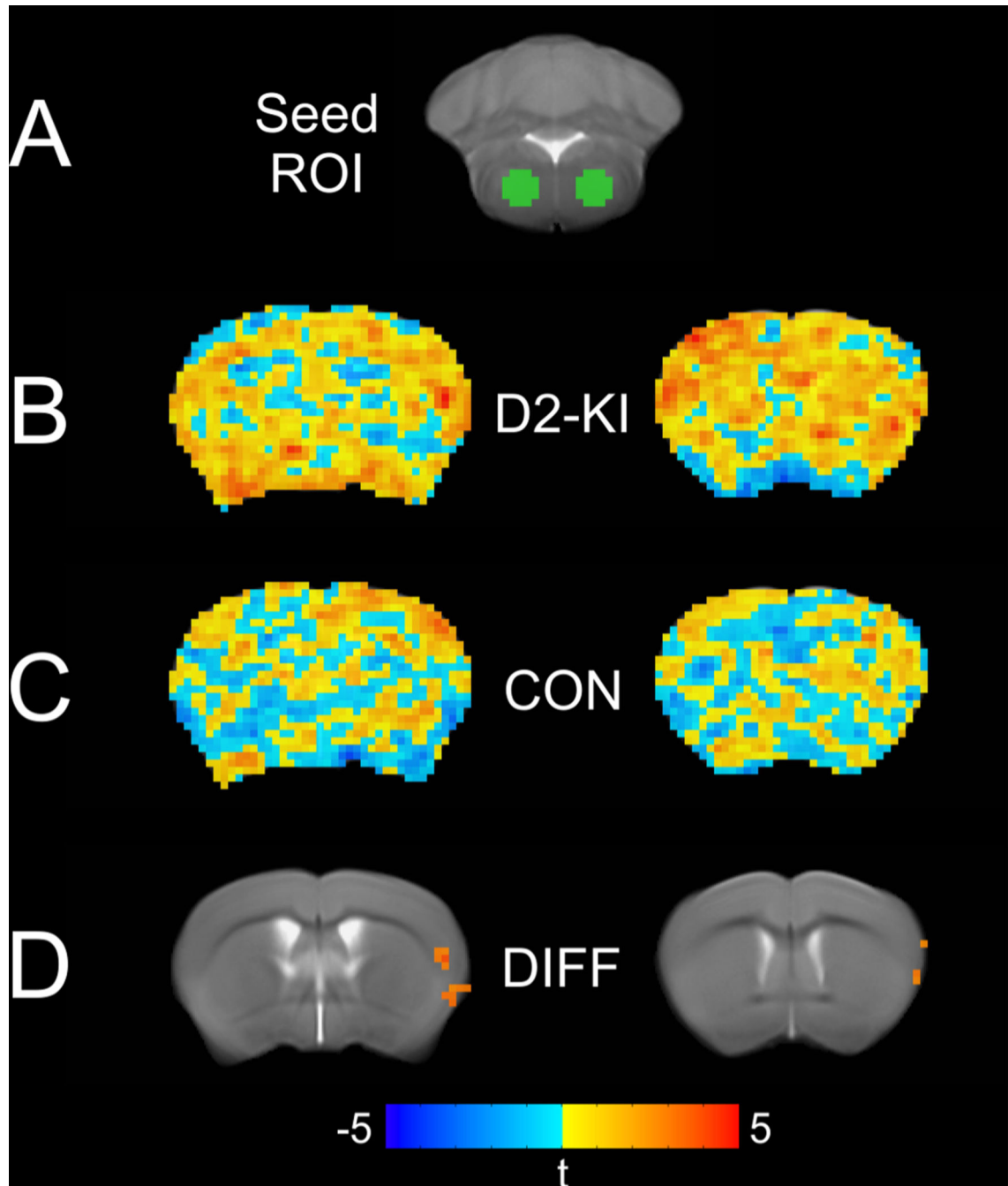
Figure 6. D2-KI resting-state functional connectivity.
Coronal slices representing functional connectivity from the anterior medulla seed (A).
Group means are shown for D2-KI mutant mice (B) and control mice (C). Red colors show
voxels with a high degree of functional connectivity and blue colors show voxels with low
degree of functional connectivity. We observed significant differences ($p_{corrected} < 0.05$)
in functional connectivity between D2-KI mutant and control mice, such that mutants had
increased functional connectivity between the anterior medulla and a voxel cluster in the
secondary somatosensory cortex (D).
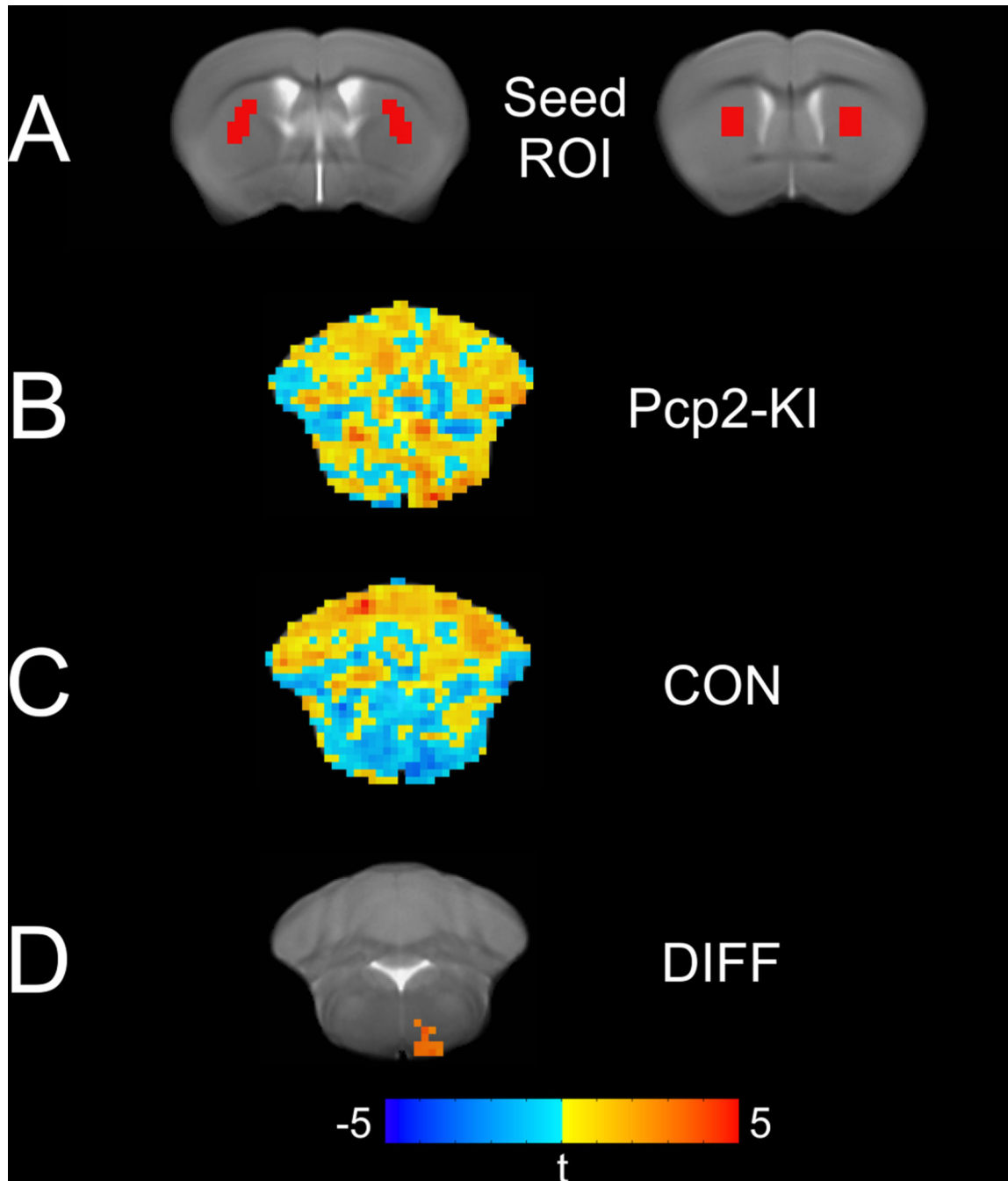
Figure 7. Pcp2-KI resting-state functional connectivity.
Coronal slices representing functional connectivity from the striatum seed (A). Group means are shown for Pcp2-KI mutant mice (B) and control mice (C). Red colors show voxels with a high degree of functional connectivity and blue colors show voxels with low degree of functional connectivity. We observed significant differences ($p_{corrected} < 0.05$) in functional connectivity between Pcp2-KI mutant and control mice, such that mutants had increased functional connectivity between the striatum and a voxel cluster in the medulla (D).

Author Manuscript   Author Manuscript   Author Manuscript   Author Manuscript

Table 1.

Mean ± SEM values are reported for beam-walking and rotarod tests in both the mutant and control mice from the D2-KI and Pcp2-KI cohorts. For both the genotypes, p values for genotype differences are reported for all the animals, for male-only and female-only analyses for the final "reduced" model.

		Mutant KI Mean ± SEM	Control Mean ± SEM	Genotype p value	Male only genotype p value	Female only Genotype p value
D2-KI	Beam-walking	0.358 ± 0.141	0.186 ± 0.052	0.039*	0.153	0.077
	Rotarod	101.73 ± 6.012	108.02 ± 4.956	0.356	0.637	0.100
Pcp2-KI	Beam-walking	0.086 ± 0.019	0.058 ± 0.017	0.245	0.063	0.809
	Rotarod	126.55 ± 5.980	111.01 ± 6.091	0.069	0.558	0.023*

Table 2.

Region of interest analysis for diffusion MRI measures of FW and FA_T in D2-KI (A) and Pcp2-KI (B) cohorts. Left column contains results for free water (FW) and right column contains results for free water corrected fractional anisotropy (FA_T). Mean ± standard deviation, and p-value are reported.

(2A) D2-KI Study

Region of interest (ROI)	Free water (FW)				Free water corrected fractional anisotropy (FA_T)			
	D2-KI Mutant (D2Cre+/− Swap+/−) Mean ± stdev	D2-KI Control (D2Cre+/−) Mean ± stdev	Genotype p value	Sex p value	D2-KI Mutant (D2Cre+/− Swap+/−) Mean ± stdev	D2-KI Control (D2Cre+/−) Mean ± stdev	Genotype p value	Sex p value
Cerebellum	0.283 ± 0.029	0.282±0.029	0.683	0.872	0.183 ± 0.026	0.185 ± 0.028	0.904	*0.013
Vermis	0.271 ± 0.029	0.272±0.028	0.950	0.598	0.195 ± 0.034	0.200 ± 0.030	0.882	0.176
pMedulla	0.306 ± 0.026	0.309±0.034	0.654	0.676	0.211 ± 0.036	0.220 ± 0.040	0.742	0.006
aMedulla	0.289 ± 0.026	0.289±0.027	0.923	0.461	0.210 ± 0.028	0.220 ± 0.032	0.222	0.363
Pons	0.292 ± 0.023	0.285±0.022	0.101	0.930	0.233 ± 0.030	0.228 ± 0.024	0.353	0.958
Midbrain	0.302 ± 0.020	0.308±0.029	0.959	0.703	0.335 ± 0.027	0.335 ± 0.024	0.808	0.078
Thalamus	0.296 ± 0.015	0.292±0.021	0.294	0.298	0.235 ± 0.045	0.230 ± 0.039	0.918	0.421
GP	0.282 ± 0.029	0.281±0.028	0.731	0.945	0.312 ± 0.058	0.325 ± 0.061	0.567	0.835
Striatum	0.270 ± 0.016	0.269±0.024	0.469	0.324	0.189 ± 0.022	0.188 ± 0.025	0.877	0.116
M1	0.273 ± 0.018	0.274±0.025	0.652	0.612	0.178 ± 0.020	0.185 ± 0.024	0.242	0.940
SS	0.272 ± 0.020	0.271±0.026	0.453	0.812	0.136 ± 0.018	0.138 ± 0.018	0.828	0.139
SNr	0.320 ± 0.013	0.318±0.023	0.418	0.846	0.343 ± 0.029	0.333 ± 0.023	0.068	***0.001

(2B) Pcp2-KI study

Region of interest (ROI)	Free water (FW)					Free water corrected fractional anisotropy (FA_T)				
	Pcp2-KI Mutant (Pcp2Cre+/− Swap+/−) Mean ± stdev	Pcp2-KI Control (Pcp2Cre+/−) Mean ± stdev	Genotype p value	Sex p value	Genotype * Sex p value	Pcp2-KI Mutant (Pcp2Cre+/− Swap+/−) Mean ± stdev	Pcp2-KI Control (Pcp2Cre+/−) Mean ± stdev	Genotype p value	Sex p value	Genotype * Sex p value
Cerebellum	0.297 ± 0.035	0.303 ± 0.037	0.374	0.766	0.327	0.197 ± 0.029	0.209 ± 0.038	0.139	**0.001	0.556
Vermis	0.283 ± 0.038	0.281 ± 0.038	0.886	0.922	0.183	0.217 ± 0.036	0.225 ± 0.039	0.367	0.372	0.124
pMedulla	0.315 ± 0.028	0.322 ± 0.033	0.379	0.600	0.218	0.219 ± 0.029	0.225 ± 0.036	0.580	***0.000	0.650
aMedulla	0.305 ± 0.042	0.311 ± 0.083	0.518	0.139	0.166	0.239 ± 0.045	0.245 ± 0.052	0.511	***0.000	0.840
Pons	0.305 ± 0.033	0.301 ± 0.035	0.778	0.332	0.269	0.247 ± 0.035	0.249 ± 0.038	0.852	*0.014	0.959
Midbrain	0.319 ± 0.027	0.313 ± 0.025	0.459	0.926	0.355	0.348 ± 0.029	0.339 ± 0.028	0.239	**0.007	0.474
Thalamus	0.308 ± 0.028	0.308 ± 0.027	0.978	0.778	0.573	0.204 ± 0.035	0.206 ± 0.039	0.940	0.536	0.190

(2B) Pcp2-KI study

	Free water (FW)					Free water corrected fractional anisotropy (FA $_T$)				
Region of interest (ROI)	Pcp2-KI Mutant (*Pcp2Cre+/− Swap+/−*) Mean ± stdev	Pcp2-KI Control (*Pcp2Cre+/−*) Mean ± stdev	Genotype p value	Sex p value	Genotype * Sex p value	Pcp2-KI Mutant (*Pcp2Cre+/− Swap+/−*) Mean ± stdev	Pcp2-KI Control (*Pcp2Cre+/−*) Mean ± stdev	Genotype p value	Sex p value	Genotype * Sex p value
GP	0.306 ± 0.028	0.304 ± 0.024	0.922	0.703	0.270	0.369 ± 0.067	0.346 ± 0.062	0.357	0.951	0.346
Striatum	0.291 ± 0.029	0.289 ± 0.024	0.868	0.777	0.984	0.189 ± 0.028	0.190 ± 0.028	0.663	0.539	0.999
M1	0.297 ± 0.027	0.297 ± 0.022	0.953	0.768	0.637	0.187 ± 0.025	0.198 ± 0.026	0.104	0.105	0.968
SS	0.296 ± 0.029	0.294 ± 0.024	0.908	0.771	0.666	0.153 ± 0.026	0.156 ± 0.026	0.600	*0.043	0.888
SNr	0.333 ± 0.018	0.329 ± .0019	0.502	0.490	0.525	0.347 ± 0.029	0.339 ± 0.026	0.235	***0.000	0.775

Abbreviations: anterior medulla (aMedulla); posterior medulla (pMedulla), globus pallidus (GP), primary motor cortex (M1), sensorimotor cortex (SS), and substantia nigra (SNr).